# Chapter 2
# Mercury's Interior

## 2.1 Mercury's Composition and Its Significance

MESSENGER has obtained the first direct compositional measurements of Mercury, measurements that are essential as a basis for constraining the planet's bulk composition and origin. The relatively unconstrained composition of Mercury allowed for a wide range of formation models (Fig. 2.1, Table 2.1) for not only the planet but also the Solar System (Clark 2007). Now that range is considerably reduced in a somewhat surprising direction, implying that enstatite chondrite is the closest 'match' among proposed models.

Table 2.2 summarizes our current assessment of Mercury's bulk and major terrain composition based on MESSENGER XRS, GRS, and neutron spectrometer measurements of elemental abundances (Weider et al. 2012, 2014; Nittler et al. 2011; Evans et al. 2012; Peplowski et al. 2012a, b; Stockstill-Cahill et al. 2012). Elemental and mineral abundance maps and regional averages derived from these instruments are described below.

Some of the most compelling findings are:

1. Relatively high Mg (magnesium) and Mg silicates, but low to moderate total iron and low Fe (iron) silicates combined with a large, dense iron-rich core implied by both density measurements and the presence of a confirmed dynamo.
2. Low Al (aluminum) but moderate Ca (calcium) correlated with Mg abundance and found along with Mg in silicates and sulfides.
3. Elevated volatile abundances including S (sulfur), Na (sodium), and K (potassium) on the surface and in the atmosphere, as well as the presence of ices and sulfides.

Enstatite chondrites, a meteorite class represented by the Abee Meteorite postulated to be an impact breccia from Mercury (Griffin et al. 1992), are the most reduced chondrites, characterized by high metallic iron (20–30 %) and low abundances of iron-bearing silicate (< 5 %). Chondrules contain very magnesian enstatite. However, the inner Solar System has no clear asteroid 'parent' that can be linked to Mercury.



P. E. Clark, *Mercury's Interior, Surface, and Surrounding Environment*,
SpringerBriefs in Astronomy, DOI 10.1007/978-1-4939-2244-4_2

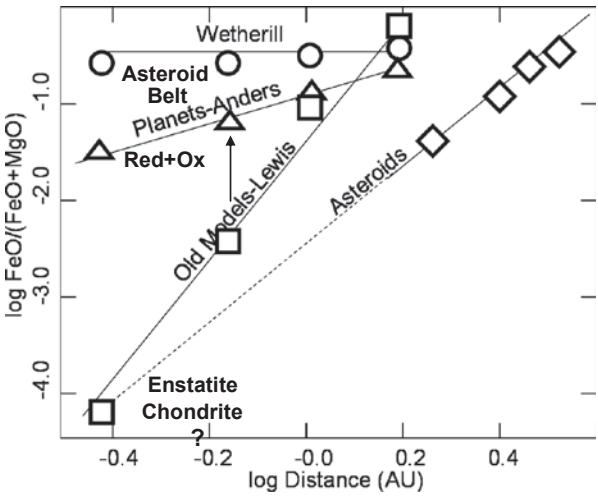


**Fig. 2.1** Wide range of formation models possible with unconstrained Mercury composition. (Courtesy of Ken Goettel 1988, unpublished figure)

**Table 2.1** Planetary formation model implications for bulk composition

| Planetary formation model | Elements | | | | | | |
|---|---|---|---|---|---|---|---|
| | Mg | Fe | Si | Na (alk) | Al (refr) | Th (resid) | S (vol) |
| (EQ) equilibrium condensation | H | LL | M | L | L | H | L |
| (SA) selective accretion | ML | MH | L | H | MH | H | M |
| (TV) t tauri vaporization | M | ML | L | L | HH | HH | L |
| (GI) giant impact | ML | MH | L | M | L | L | L |
| (RO) reduced/ oxidized | L | H | M | L | L | L | M |
| (EC) enstatite chondrite | H | M | H | H | L | L | H |

*H* high, *M* moderate, *L* low
*EQ* Lewis Heliocentric distance dependent temperature, *SA* selection of metals versus silicates due to aerodynamic/mechanical properties, *TV* removal of large fraction of silicate mantle and volatiles due to T Tauri event, *GI* removal of large fraction of silicate mantle and volatiles due to giant impact, *RO* Anders reduced (metal enriched) followed by provenance-dependent incorporation of oxidized (silicate enriched) components, *EC* reduced chondritic composition at Mercury provenance

The compositions of major terrains, indicative of major episodes of geochemical differentiation, are shown in Table 2.2. The older, intercrater plains/highly cratered terrain (IcP/HCT) is richer in Mg and lower in Fe, implying a higher temperature melt, as indicated by spatially resolved measurements of Mg/Si, Al/Si, S/Si, and Ca/Si for the northern volcanic plains. Early volcanism involving deposition of this

**Table 2.2** XRS- and GRS-derived bulk and major terrain composition

| Abundance | Source | Bulk | ICP/HCT | NVP | CB |
|---|---|---|---|---|---|
| *XRS-derived* | | | | | |
| Mg/Si | Weider et al. 2012 | | 0.57 | 0.34 | |
| S/Si | Weider et al. 2012 | | 0.09 | 0.06 | |
| Ca/Si | Weider et al. 2012 | | 0.19 | 0.15 | |
| Fe/Si | Weider et al. 2014 | 0.06 | | | |
| Al/Si | Peplowski et al. 2012b | | 0.22 | 0.26 | |
| Mg | Weider et al. 2012 | | 14.4 | 8.6 | |
| Fe | Weider et al. 2014 | 1.5 | | | |
| Ca | Weider et al. 2012 | | 4.9 | 3.7 | |
| S | Weider et al. 2012 | | 2.3 | 1.5 | |
| Al | Weider et al. 2012 | | 5.4 | 6.6 | |
| *GRS-derived* | | | | | |
| S/Si | Evans et al. 2012 | 0.092 | | | |
| Ca/Si | Evans et al. 2012 | 0.24 | | | |
| Fe/Si | Evans et al. 2012 | 0.077 | | | |
| Al/Si | Peplowski et al. 2012b | 0.25 | | | |
| Na/Si | Evans et al. 2012 | 0.12 | | | |
| Si | Evans et al. 2012 | 24.6 | | | |
| Mg | Peplowski et al. 2012b | 12.2 | | | |
| Fe | Evans et al. 2012 | 1.9 | | | |
| Ca | Evans et al. 2012 | 5.9 | | | |
| S | Evans et al. 2012 | 2.3 | | | |
| Al | Peplowski et al. 2012b | 5.7 | | | |
| Na | Evans et al. 2012 | 2.9 | | | |
| O | Peplowski et al. 2012b | 48.9 | | | |
| K | Peplowski et al. 2012a | 1200 ppm | 952 ppm | 1786 ppm | 754 ppm |
| Th | Peplowski et al. 2012a | 0.16 ppm | 0.168 ppm | 0.142 ppm | 0.54 ppm |
| U | Peplowski et al. 2012a | 90 ppb | | | |
| Ti | Rhodes et al. 2011 | 1.2 | | | |
| Si | Rhodes et al. 2011 | 18 | | | |

% abundance and abundance ratios by weight

material was followed by two episodes of smooth plains (SP) formation, which apparently overlapped with northern plains formation. Fe progressively substituted for Mg as the interior cooled during a successively lower temperature melting process. The observed relatively high Na abundance is consistent with the presence of Na-bearing plagioclase feldspar inferred from ground-based spectral measurements (Sprague and Massey 2007).

## 2.2 Geochemical Differentiation

Either Mercury accreted from source material similar to enstatite chondrites but with higher bulk Fe or the enstatite chondrite parent body and Mercury accreted independently from material of similar composition, in terms of bulk abundances, mineralogy, and isotope compositions. In either case, a high degree of partial melting of a very reduced source and crystallization of basalts would have occurred subsequently. The composition of Mercury surface material is apparently more similar to basaltic melt derived from an enstatite chondrite-like source region rather than to residual silicates such as aubrites, particularly in regard to the widespread presence of sulfides (Weider et al. 2012).

High surface S combined with low oxygen fugacity implies accretion from reduced materials such as enstatite chondrites, which might also have been subjected to loss and depletion of iron sulfide resulting from evaporation of troilite in the inner nebula (Zolotov et al. 2013). Models of the geochemical differentiation process (Zolotov et al. 2013) based on these findings indicate that calcium and magnesium sulfides would be common in volcanic rocks, and oxygen fugacities would be low in parent magmas. Zolotov and coworkers (2013) evaluated resulting oxygen and sulfur fugacities as well as resulting silicate/sulfide equilibria using empirical models for silicate and metallurgical slag formation. The predicted range of oxygen fugacities (IW-4.5–7.3@1700–1800 K) (Zolotov et al. 2013) has implications for the differentiation process. Resulting values of Fe in silicate correspond to 0.03–0.79 weight percent FeO, below the detection limit of reflectance measurements, are consistent with reducing conditions, lower oxygen fugacities, and partial melt of enstatite chondrite. These conditions imply the presence of iron in sulfides, also suggested by the correlation between Fe and S. Low oxygen fugacities and reducing conditions, combined with the presence of S constrain oxidation states, increase sulfur solubility and induce more 'chalcophile' behavior (bonding with S) among typically 'lithophile' (bonding with Si) elements, including Mg, Ca, Ti, Na, and K, as well as U and Th, and thus affect metal/silicate partitioning (Keil 1968).

Abundances of major rock-forming elements (Mg, Al, Ca, Si) also indicate a high degree of partial melting implying substantial heat production in the mantle (Peplowski et al. 2011) (Table 2.2). Extensive early volcanism followed by episodic volcanism supports core formation-induced crustal expansion, followed by slow cooling, and finally core partial solidification induced crustal contraction. Implied bulk compositions are most similar to Mars meteorites, depleted in incompatible elements (Peplowski et al. 2011).

Peplowski and coworkers (2011, 2012a) GRS-derived average surface abundances for radioactive elements K, Th, and U (Table 2.2) are consistent with chondritic source from high temperature nebular condensates but, based on the K/Th ratio, with considerably greater volatile abundances than conventionally associated chondritic material. Observed U/Th ratios are slightly less than inner planetary and chondritic averages (Peplowski et al. 2011), indicating some separation of U (uranium), thus somewhat lower oxygen fugacity and reducing conditions, because U and Th (thorium) are not separated under more oxidizing conditions. However, U and

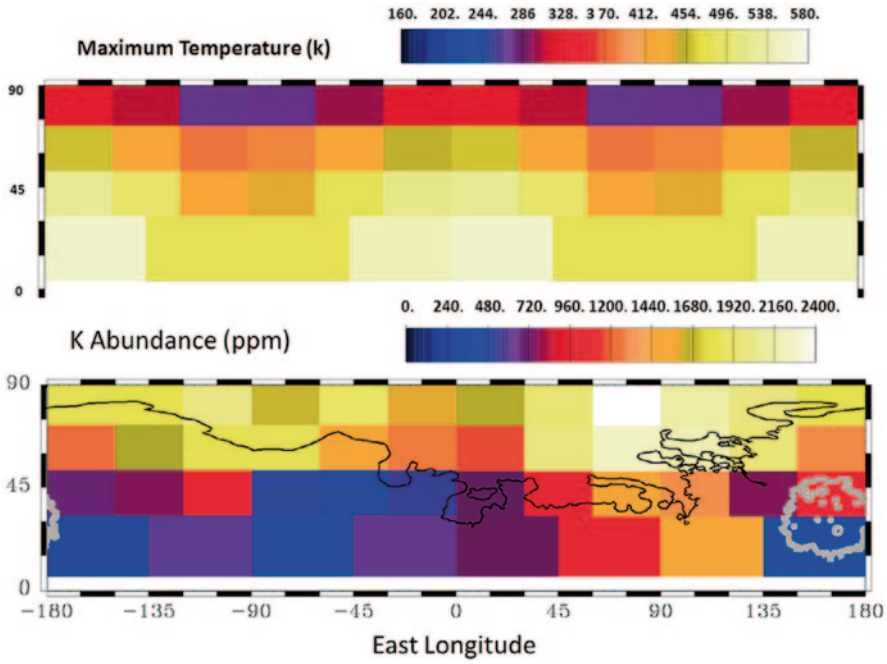


**Fig. 2.2** Comparison of maximum temperature (*top*) and K abundance (*bottom*) from 0 to 90 degrees latitude (*vertical axis*) and all longitudes (*horizontal axis*). (Peplowski et al. JGR Planets 2012a, Fig. 11b (*top*) and 8a (*bottom*), © 2012 American Geophysical Union)

Th abundances on Mercury are comparable to terrestrial oceanic basalts (Peplowski et al. 2011), limiting the extent to which reducing conditions and sequestration of these elements with heavy element sulfides occur in the core. Thus, although K/Th ratio is higher than inner planetary and chondritic averages, that ratio can't be explained by extensive core sequestration of Th but is more likely to result from thermal redistribution of K near the surface. In addition, models based on these bulk abundances indicate not only considerable internal heating but for a period four times longer than previously thought, with not enough heat production from incompatible radioactive elements (U, Th) to drive core convection (Peplowski et al. 2011, 2012a). K, Th, and U abundances are thus consistent with a model for widespread volcanism following the late heavy bombardment, gradually declining internal heat production and with less extensive episodes of volcanic activity subsequently (Fig. 2.2). McCubbin and coworkers (2012) also interpreted GRS and XRS-derived K, Th, U, and S abundance values to be indicative of a higher reducing environment with very low oxygen fugacity and higher volatile abundances than previously assumed. They pointed out that an important indicator of the volatile depletion during formation is the ratio of very large ion lithophiles (LIL) that are relatively volatile (e.g., K) to those that are more refractory (U, Th, rare earths). U and Th partitioning into the metal rich core and the sulfide oldhamite ([CaMgFe]S),

which can be inferred from S abundance measurements, is not enough to account for the high K/Th and K/U ratios. On the other hand, the addition of a FeS layer between the mantle and core, proposed as an insulating solid cap to maintain thermal conditions necessary to sustain the dynamo that will be discussed soon, could account for these ratios and allow for a volatile-rich Mercury.

The presence of the nickel-iron (siderophile) group elements and Ti (titanium), as well as alkalkis (K and Na), constrain the petrology of Mercury's magmas. The low percent of FeO (in silicates) by weight in the model is lower than total iron abundances determined from XRS and GRS measurements, and thus must also be present as iron sulfides, primarily troilite, and metal, which could have crystalized and separated from cooling magmas. All but the lowest part of the range of predicted oxygen fugacity values are consistent with an Fe core enriched in Si and/or S and capable of forming the proposed solid FeS shell discussed (Smith et al. 2012).

S content itself may reflect the heterogeneity in the redox environment, e.g., greater sulfur abundances at higher temperatures (Weider et al. 2012). Somewhat lower Mg and So abundances of the northern volcanic plains could be explained by a somewhat lower degree of partial melting than the oldest terrains. A lower subsurface temperature could allow partial oxidation of sulfide and formation of native sulfur. As temperature and solubility decrease, outgassing of S, N (nitrogen), and C (carbon) could lead to the observed pyroclastic activity (Kerber et al. 2009, 2011). However, the observed effusive style of volcanic activity for many melts apparently indicate a minor role for outgassing resulting from assimilation of crustal S (Head et al. 2011).

Despite the presence of sulfides and immiscibility of silicate and sulfide melts, the predominance of silicates combined with their far higher temperatures of crystallization would not be consistent with large-scale separation and flotation of less dense Ca and Mg sulfides on the silicate magmas (Zolotov et al. 2013; McCoy et al. 1999). Instead these sulfides, combined with Fe, were embedded in the accreting material, and distributed as late stage crystallization products in erupting magmas. Dense Fe-S rich melts, on the other hand, would sink, ultimately forming a mantle sublayer (Smith et al. 2012).

Ebel and Alexander (2011) have pointed out that solids likely to survive in the accretion zone of Mercury would be similar to highly unequilibrated anhydrous interstellar organic and presolar grains with porous interplanetary dust particles of chondritic composition (C-IDP) as follows. High temperature reactions with these compositions produce condensates (solid plus liquid assemblages in equilibirium with vapor) with greater than chondritic Fe/Si ratios that are about half of the Fe/Si estimated for the bulk composition of Mercury. Stable minerals include FeO-poor enstatite chondrites, with S behaving as a refractory element at lower temperatures. Local compositional gradients in volatiles of the accreting disk, due to 'cold finger' effects (Stevenson and Lunine 1988), combined with an efficient metal/silicate fractionation process, could create enstatite parent body compositions and explain Mercury's anomolous (high S, very low FeO, high metallic Fe) composition. The condensing Mg-rich olivine in C-IDP systems removes oxygen, progressively decreasing oxygen fugacity and FeO content They reduce even more as the

temperature decreases, in direct contrast to hydrous silicate-rich CI systems. Eventually enstatite predominates over olivine, creating the basis for Mercury's low Fe silicate composition with a metallic iron core. In Mercury's neighborhood, unlike the neighborhoods of other terrestrial planets, the presence of C-IDP dust resulted in sulfur in refractory rather than vapor phases (Ebel and Alexander 2011). Thus, Ca occurs with S rather than Al, as it does in oxidized systems. Si rather than Fe is more volatile over a broader temperature range, resulting in a high bulk Fe/Si ratio. If this model is correct, Mercury should be relatively organic rich and hydrogen poor, reflecting the I-CDP composition.

## 2.3 Surface Composition and Its Implication for Interior Processes

The distributions of GRS measurement-derived elements (Table 2.2) are dissimilar (Peplowski et al. 2012a, b). Th, Si, and O vary little. K is anti-correlated with maximum surface temperatures, varying from 300 to 2400 ppm in the northern hemisphere, and thus apparently controlled thermally, lost to the exosphere where it has been observed (Ref). Its higher value for the northern volcanic plains would be consistent with their location around a 'cold pole' described earlier (Fig. 2.2). The decrease in K/Th is consistent with thermally induced diffusion rates in alkali-bearing feldspars. Another clue substantiating K loss is the pattern of minimum Na/K ratio at the subsolar point, which is consistent with a photo sputtering rate for K twice that of Na and K's far longer lifetime before ionization. Exospheric Na is 250 times greater on Mercury than on the Moon, whereas exospheric K is only 93 times greater on Mercury, although K is far more enhanced at warm longitudes.

On the other hand, K/Th ratios could show a different relationship for different episodes of volcanism as they do on the Moon (Fig. 2.3). The highest K and Th on the Moon are associated with the oldest volcanic basalts, with lower abundances and considerable variation found in earlier crustal rocks. However, temperature differences as opposed to compositional differences are likely to account for most of the variations in surface K on Mercury.

XRS and GRS derived Fe/Si and Ti/Si ratios (Table 2.3) are consistent with values estimated from the neutron spectrometer. GRS Si abundance estimates are consistent with the earlier observations from ground-based IR measurements that Mercury rocks have slightly less Si than lunar rocks (Sprague and Massey 2007). However, little Fe and virtually no Ti are observed, contrary to earlier interpretations of color observations indicative of high Ti basalts. Thus, FeTi oxide abundances would be insufficient to account for neutron absorption inferred from the neutron spectrometer. Because additional metallic Fe in nanophase iron or elsewhere isn't compatible with the presence of FeO-rich ilmenite, Riner and coworkers (2010) had proposed rhombic oxide $MgTiO_3$ (egelkelite), which could be produced by partial melting of metal-rich enstatite chondrite (Brown and Elkins-Tanton 2009) as an alternative, a possibility that is still excluded by the extremely low Ti abundances.

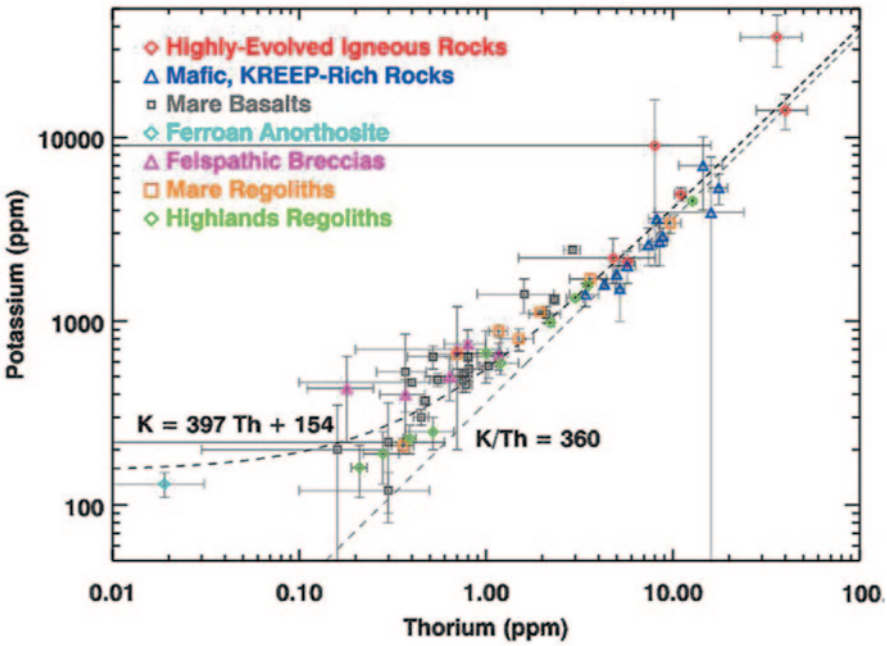


**Fig. 2.3** Relationship between lunar K and Th indicating K retention relative to Th for lower Th rocks. Mercury has a low Thorium bulk abundance. Peplowski et al., JGR Planets, 2012, Figure 10, ©2012 American Geophysical Union.

**Table 2.3** Dynamic figure parameters

| Parameter | Value | Error | Source |
|---|---|---|---|
| Radius | 2439 km | 0.69 | Oberst et al. 2011 |
| Crust and mantle depth | 410 km | | Hauck et al. 2013 |
| Depth to liquid core | 420 km | | Hauck et al. 2013 |
| Spin axis | 2.04 arc min | 0.08 arc min | Margot et al. 2012 |
| Forced libration amplitude | 38.5 arc sec | 1 arc sec | Margot et al. 2012 |
| Forced libration displacement | 450 m | 10 m | Margot et al. 2012 |
| $C/MR^2$ | 0.346 | 0.014 | Margot et al. 2012 |
| $C_M/C$ | 0.431 | 0.025 | Margot et al. 2012 |
| $C_{20}$ dynamic oblateness | $2.24 \times 10^{-5}$ | $0.01 \times 10^{-5}$ | Smith et al. 2012 |
| $C_{22}$ dynamic ellipticity | $1.253 \times 10^{-5}$ | $0.01 \times 10^{-5}$ | Smith et al. 2012 |

Mercury has a distinctive and anomalous surface composition. Crustal iron is correlated with magnetization contrast in all the terrestrial planets except Mercury (Purucker et al. 2009). Weider and coworkers (2014) mapped average XRS Fe/Si ratio measurements taken during 55 solar flares (Fig. 2.4) and an estimated bulk iron abundance of 1.5% from these measurements. Most of the measurements

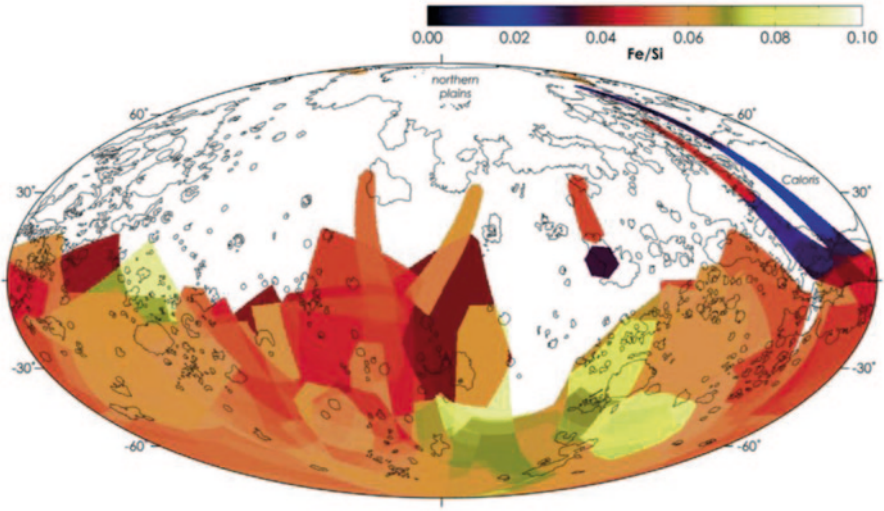


**Fig. 2.4** Map of XRS-derived Fe/Si measurements taken during times of solar flares. Reprinted from Icarus, 235, Weider et al, Figure 10a, ©2014, with permission from Elsevier.

included in the study were taken from the southern hemisphere when the spacecraft was further away from the planet and areas of coverage were larger. Thus, we have little coverage for the more extensively studied volcanic deposits in the northern hemisphere. Attempts were made to correct measurements for differences in phase angle. Corrected measurements, with a 10% intrinsic error, vary by two standard deviations form the average across the southern hemisphere. Significantly, larger variations in Fe/Si are observed for more spatially resolved, smaller footprint areas. Largest Fe/Si ratios, potentially indicating larger iron metal and iron sulfide deposits, are found in the southern hemisphere associated with 'blue' areas.

The relatively high Mg/Si and low Al/Si and Ca/Si ratios clearly indicate Mercury does not have a lunarlike crust, and the sulfur abundance makes it substantially more chondritic than the Moon and terrestrial planets (Table 2.2). These data, combined with the low surface iron and iron silicate abundances, suggest highly reduced parent material such as enstatite chondrite or anhydrous dust particles, although additional metal/silicate fractionation in the solar nebular may be necessary to explain Mercury's bulk composition. Surface composition ranges from ultramafic to basaltic and most closely resembles terrestrial komatiites, which could have formed from a high degree of partial melting of the proposed parent material. These measurements and proposed parent material are consistent with the presence of Mg- and Ca-rich sulfides as opposed to FeS as the dominant form of sulfur in the crust. The presence of sulfur would support the development of pyroclastics during volcanic activity. Low Ti and Fe do not support the conventional model for space weathering based on the darkening of opaque oxides, although high surface temperatures and aggressive particle bombardment could support formation of agglutinates. Low reflectance, particularly associated with areas of the highest Mg/Si, Ca/Si, and S/Si,

may be due to the presence of sulfides as opposed to conventional space weathering associated with the Moon.

Major terrains of Mercury have distinctive signatures (Weider et al. 2012, 2014) as follows. High Mg mafic minerals, plagioclase feldspar, and smaller amounts of Ca, Mg, and/or Fe sulfides are the major minerals reflecting a high degree of partial melting of an enstatite chondritic source. Older terrain is higher in XRS-derived Mg/Si, S/Si, Ca/Si and lower Al/Si ratios than younger, smoother plains. Compositional differences could result from crystallization of smooth plains from a more evolved magma source. The younger Caloris plains that would result from crystallization of a more evolved magma source can be readily distinguished from the older northern volcanic plains (Fig. 2.4). However, although substitution of Fe for Mg in Mg-depleted source regions in younger volcanic units is likely, Fe abundances of these units are still higher than enstatite chondrite melts should allow, indicating an additional source, such as an exogenous contribution from meteorites. Visible/near IR measurements can distinguish smooth plains (higher reflectance, from intermediate and low reflectance units on the basis of spectral slope, reflectivity, and morphology) (Denevi et al. 2009). The two clusters of the oldest terrain (IcP-HCT) have higher Mg/Si, S/Si, Ca/Si, and lower Al/Si than the northern plains. One cluster has somewhat more moderate Mg/Si and Al/Si. The oldest terrain is most compositionally analogous to terrestrial ultramafic komatiites, but with a larger range of composition than seen in terrestrial midoceanic ridge basalts.

Mg and Fe compositions are consistent with Mg-rich pyroxene (enstatite) and olivine (forsterite), and Ca/Si and S/Si ratios are most consistent with the sulfide oldhamite (Weider et al. 2012, 2014), which has been identified by Sprague and coworkers (1995) from ground-based IR observations and is found in enstatite chondrites and achondrites. Most of the Ca is probably in plagioclase feldspar, but the lack of correlation with Al indicates that Ca must be found in minerals other than calcic plagioclase as well, including sulfides and non-sulfides such as diopside, which has also been identified by Sprague and coworkers (2002). Ca may also be found in Ca-rich pyroxene, but that would not account for the higher Al/Si ratios for the younger northern volcanic plains, indicating that some of the Al must be found in Na- or K -ich feldspars, as inferred from GRS observations (Peplowski et al. 2012a, b), although variations in K are related to surface heating.

The bimodal composition of IcP/HCT terrain could suggest that the crust is heterogeneous (Weider et al. 2014). The two distinct lithologies are ultramafic with enstatite and some plagioclase and oldhamite and basalt with some sulfide content (more like the northern plains material). Lower Mg of the younger material suggests derivation from more differentiated and cooler magma from which higher Mg mafics have already crystallized, producing a composition more like mid-oceanic ridge basalts (MORB). If the younger northern plains and Caloris Basin smooth plains resulted from remelting of the older basalt source region, the trends in composition would parallel komatiite-MORB trends, but this is not the case (Fig. 2.5). The more likely scenario is that the two terrains originated from different portions of the mantle, the earlier at higher temperature and greater partial melting, and the latter at lower temperature due to slow cooling and thus a lesser degree of partial melting.

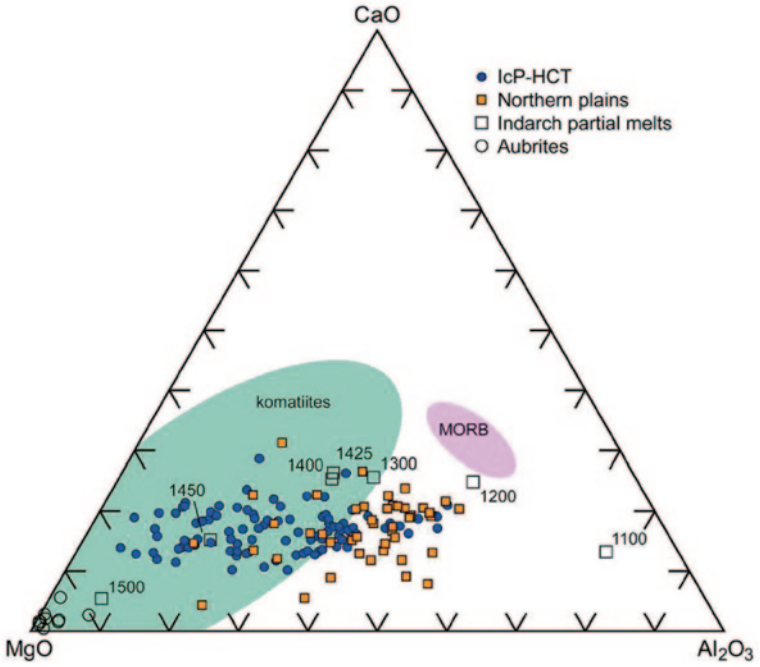


**Fig. 2.5** MgO-Al2O3-CaO ternary diagram illustrating relationship between older IcP-HCT and northern plains volcanic units, enstatite chondrite partial melt ( Indarch), aubrite meteorites, and terrestrial ultramafic ( komatiites) and mafic ( MORB) rocks.(Weider et al. JGR Planets 2012, Fig. 6, © 2012 American Geophysical Union)

Mercury mineral compositions and abundances have been derived using petrological modeling of Mg-rich magmatism under reducing conditions assumed on the basis of bulk compositional estimates for Mercury (Stockstill-Cahill et al. 2012). The MELTS model, typically used for terrestrial applications, was modified for Mercury conditions by assuming a lower initial iron content and removing sulfur, on the basis that it would form sulfides; corresponding mole fractions of Mg and Ca were removed. The resulting models indicated that the closest analog for Mercury rocks would be magnesian basalt composed of Mg-rich orthopyroxene and plagioclase (Fig. 2.6).

## 2.4 Thermal Considerations and Implications for the Interior

A variety of measurements provided by MESSENGER have yielded constraints for the thermal evolution of Mercury (Michel et al. 2013). Surface Mg and S abundances are consistent with high interior temperatures and a high degree of partial melting

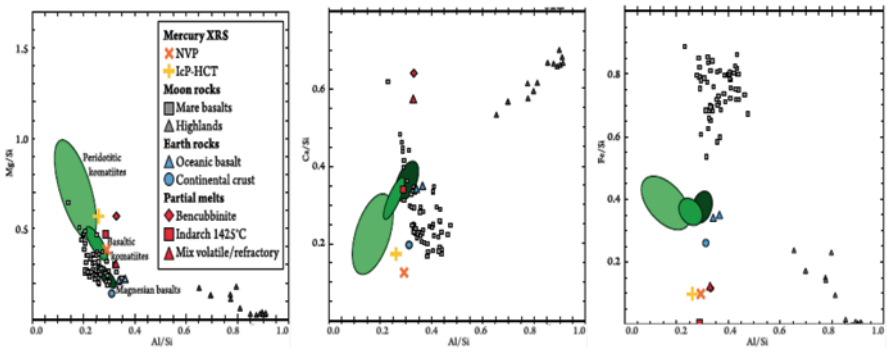


**Fig. 2.6** MELTS models of Mercury rock type and major minerals derived from relationships between Mg/Si, Fe/Si, Ca/Si, and Al/Si. Stockstill et al., JGR Planets, 2012, Figure 2, © 2012 American Geophysical Union.

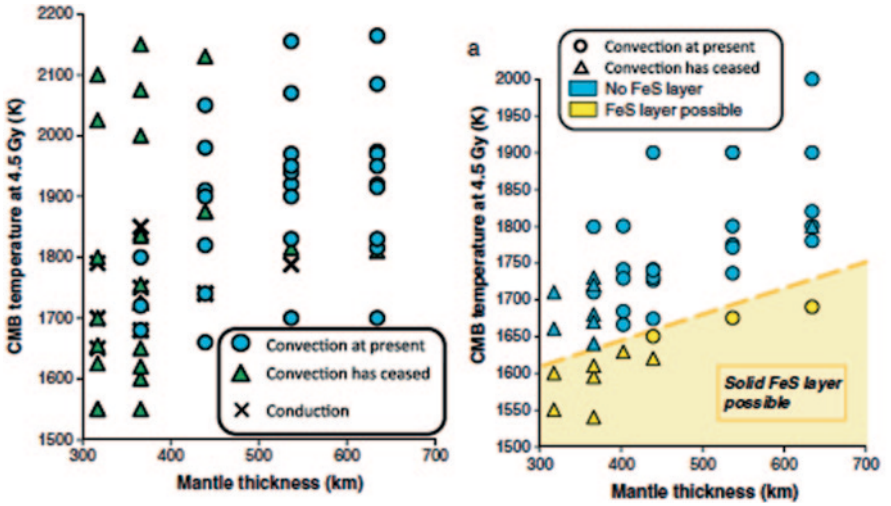


**Fig. 2.7** Model for core mantle boundary temperature versus mantle thickness, indicating ( left) convection that could persist, providing the mantle is > 400 km. Right: In the presence of a FeS outer shell a mantle of this size could remain convecting until the present. (Michel et al. JGR Planets 2013, Fig. 2 ( left) and 6a ( right), © 2013 American Geophysical Union)

in the mantle, while U, Th, and K abundances constrain the rate of radiogenic heat reduction. When these data are combined with the determinations of $C/MR^2$ and $C_M/C$ ratio (Smith et al. 2012), as described below, the implications are that Mercury's core is larger and its mantle is thinner (slightly larger than 400 km) (Hauck et al. 2013) than previously estimated. Michel and coworkers (2013) explored the possibility that convection ceased at some point, and determined that mantle convection could persist as long as the mantle is>400 km (Fig. 2.7), resulting in

widespread high temperature magmas with high degrees of partial melting. The systematic decrease in Mg and sulfides from older to younger terranes is consistent with a decrease in degree of partial melting. The presence of orthopyroxene enstatite, with its high Mg content, as a major component of volcanic deposits, doesn't preclude the presence of clinopyroxene (Stockstill-Cahill et al. 2012). However, the presence of clinopyroxene, which melts at a lower temperature than orthopyroxene and olivine, increases the degree of partial melting to the extent that it is not consistent with the observed decrease in the degree of partial melting.

The most efficient means of heat transport is convection. How well does convection work in Mercury's mantle? A thin mantle implies a low Rayleigh number (ratio between buoyancy and viscous dissipation forces that scale as the third power of the convecting layer) and marginal instability allowing convection. However, higher starting temperature and higher heat production can offset the effect of a thin mantle by lowering its viscosity. Do the large variations in externally induced surface temperature at Mercury's hot poles play a special role? Michel and coworkers (2013) argue that such variations cause larger convection cells with somewhat prolonged melting, and that this does change the thermal structure and thickness of the lithosphere. Long wavelength variations in topography resulting from variations in depth to the core mantle boundary could induce variations in boundary temperature, affecting heat flow from the core and thus the generation and morphology of the magnetic field. An outer FeS solid shell, which would result in a boundary temperature below the melting point of FeS, has been proposed to explain the greater core density than the implied by low iron content (Smith et al. 2012). Such a layer provides even greater constraint than required to explain a mantle that remains convecting over a longer period of time. Current models (Michel et al. 2013) indicate that convection continued until less than 1 billion years ago (Fig. 2.7).

Grott and coworkers (2011) generated thermal models using the best available data on Mercury's bulk composition and a thermally insulating regolith layer. These constraints provide a stiff enough mantle rheology and inefficient enough mantle convection to slow cooling and prolong production of magma until 2.5 billion years after core formation, consistent with MESSENGER observations (Prockter et al. 2010). Volume increase associated with mantle differentiation offsets contraction caused by core cooling to some extent, although an order of magnitude more contraction than observed by *Mariner 10* is required. Crustal thicknesses between 10 to 40 km and high (6 %) core sulfur contents are implied. Grott and coworker (2011) models imply a two-stage magnetic field generation after core formation. Over the first few hundred million years thermal convection occurs in the fluid core, resulting in a thermally driven dynamo. As a small inner core solidifies, the mechanism becomes the composition convection in the non-eutectic fluid outer core, a mechanism consistent with the weak magnetic field observed today (Anderson et al. 2008). Deep dynamo models (Christensen and Wicht 2008) predict such a weak field and inner core but require sulfur content that would result in early core freezing and contraction. On the other hand, recent experiments demonstrate that FeS systems might exhibit melting behavior and a crystallization regime very different from that assumed for the other terrestrial planets (Chen et al. 2008). Iron

precipitation may depend on sulfur content, and occur not just at the inner/outer core boundary but elsewhere (double snow state). Such precipitation could be a source of compositional buoyancy that could act as the 'compositional convection' driver for the weak dynamo. The observed crustal thickness is compatible with this model, which allows modest mantle convection that could continue to the present (King 2008; Redmond and King 2007). However, strictly speaking, the chondritic composition source material proposed for Mercury provides too little U and Th to be consistent with this model.

## 2.5 Surface Features and Implications for the Interior

Though the photogeological and geomorphological details of surface features will be discussed in more detail in Chap. 3, this section discusses surface structural features from the standpoint of deep interior processes.

According to Achille and coworkers (2012) MESSENGER imaging with >50 degree solar incidence angle revealed many undetected surface structures, implying greater spatial distribution and density of tectonic features and thus evidence for greater extent of compressional strain and accompanying radius decrease (2.4–3.6 km) 3–4 times higher than previous estimates.

Lu and coworkers (2011) studied the chaotic terrain area antipodal to the Caloris impact basin to provide information on Mercury's interior structure through observed effects that would have resulted from seismic focusing of waves resulting from the impact. Compression and rarefaction occur as waves propagate through the planet and crustal layer, and disruption occurs when tensile stress exceeds tensile strength. Impacts produced by both surface acoustic (Rayleigh) waves and mantle guided waves trapped between the core and the free surface caused the terrain formation. The terrain consists of 5–10-km-wide hills and depressions 0.1–0.8 km in height. The models predicted disruption zone of 5 angular degrees, but the actual disruption is more like 10 angular degrees, potentially indicating that antipodal response to the impact was modulated or magnified by the shallow outer layer of Mercury.

Caloris, the largest known impact basin on Mercury, has had a broad influence not just on Mercury's surface but potentially on the interior, by affecting heat flow within the mantle and core (Roberts and Barnouin 2013). Perhaps the thermal impulse of its formation changed the underlying dynamics of the thin mantle and was responsible for the region's subsequent volcanism. On the other hand, Roberts and Barnouin (2013) indicate that the subsequent heating could not have penetrated to the core and thus had no impact on the dynamo. The younger age of the volcanic plains around Caloris indicate that they are not impact melt. Color variations among the plains indicate a composition that evolved. Both of these conditions support a volcanic origin for the plains.

Roberts and Barnouin (2013) modeled shock heating and convection in the mantle with standard impact scalings as follows. Similar volumes of melt are produced for a given impact energy. Projectile size determines the extent of heating,

and thermal effects on the deep mantle may last for some time. Mantle composition affects density, which also affects melt behavior. Melting occurs where the temperature is hottest beneath a thick stagnant lid, and because the mantle is shallow and gravity and pressure relatively low, melting can occur at significant depth in the mantle. Prior to an impact event, a significant fraction of the lower mantle may already be melted and mixed due to ambient conditions. The impact causes a sharp rise in temperature and subsequent melting due to upwelling material undergoing decompressive melting. Impact heating is confined to the small convective cell closest to the impact site for this thin mantle, heat decaying strongly with distance, confining it to regional rather than global influence.

Impact-induced melting results in a pocket of highly depleted material below, which rises along with the heated region and spreads out along the stagnant lid (Roberts and Barnouin 2013). Thermal buoyancy exceeds chemical buoyancy, resulting in well-mixed lower mantle overlain with the strongly depleted, high viscosity lid, covered with volcanic plains around the impact site. Surrounding this area is well-mixed mantle overlain with unprocessed, undepleted stagnant lid. Pockets of depleted material have been well mixed into the mantle. There is a strong compositional contrast between basement rocks beneath volcanic plains interior to the basin and those surrounding the basin. Although most of the heat dissipates relatively quickly, the stagnant lid cause some heat to be retained for tens of millions of years. A lower mantle viscosity has a modest influence, resulting in a somewhat thinner stagnant lid, a second phase of melting at similar depth, somewhat less contrast between melt compositions and more upwellings, and a somewhat faster cooling mantle. According to Roberts and Barnouin (2013), the key influence is temperature, related to heat externally generated by impact and internally generated through radiogenic heating and not composition.

Exterior melt production is likely only for the slower, larger impacts, and the average impact velocity (42.5 km/s) is far too high for melt production (LeFeuvre and Wieczorek 2008), which come from a much deeper source than conventional impact melts and regions with different compositions, especially in terms of the highly variable Mg. Impact-induced volcanism should be systematically supressed over time as more easily melted components are depleted.

## 2.6 Figure and Dynamics of Mercury

A number of workers have improved our understanding of the figure and dynamics of Mercury from MESSENGER observations or ground-based observations taken in preparation for the mission (Table 2.3). Margot and coworkers (2012) derived better values for the spin properties, including the position of the spin axis ($2.04 \pm 0.08$ arc minutes with respect to orbit normal) from Earth-based radar observations, indicating Mercury is in or near a Cassini state. An 88-day libration pattern in the rotation rate is due to solar gravity torques acting on the asymmetrically shaped planet. Forced libration amplitude ($38.5 \pm 1$ arc sec) corresponds to 450 m

of displacement at the equator. By combining these data with second-degree gravity harmonics derived from MESSENGER measurements by Smith and coworkers (2012), Margot and coworkers (2012) determined the polar moment of inertia ($C/MR^2$) to be $0.346 \pm 0.14$ (where C is the moment of inertia, M as the mass, and R is the radius of Mercury), and the fraction of that moment of inertia corresponding to the outer librating shell ($C_M/C$), from which the size of the core can be estimated, is thought to be $0.431 \pm 0.025$ (where $C_M$ is the moment of inertia of the outer rigid shell only). This model assumes that the core mantle boundary and inner core boundary are axially symmetric, although convective or tidal processes undoubtedly cause some non-hydrostatic variations in mantle density that, as Gao and Stevenson (2012) suggest, could affect inferred mantle densities by 10–20%.

A number of workers have provided new measurements for Mercury's radius and interpretations for variation in its radius. From MESSENGER measurements, Oberst and coworkers (2011) estimate the radius as $2439 \pm 0.69$ km, and a nearly identical radius for equatorial and polar radii, suggesting negligible gravitational oblateness and topography rather than gravitational oblateness as the source of uncertainty. Perry and coworkers (2011), using MESSENGER radio occultation, estimated the radius as $2439.2 \pm 0.5$ km. An offset of Mercury's equatorial plane from the center of figure 600 m has been suggested (Anderson et al. 1996; Smith et al. 2010). RMS roughness obtained from these limb observations (0.8) is comparable to that obtained from laser altimetry (0.9) (Oberst et al. 2011). The large regional depression observed in the stereo terrain model may be correlated with a 1500 km impact basin (Preusker et al. 2011).

## 2.7 Gravity Anomalies

Smith and coworkers (2010, 2012) derived Mercury's northern hemisphere gravity field (Table 2.3, Fig. 2.8), but because of the high northern latitude periapsis resulting in poor coverage in the southern hemisphere, only a long wavelength field in the southern hemisphere was derived. The geoid has a dynamic range of 200 m. Several large gravity anomalies including mascons (mass concentrations similar to those found for young basins on the Moon) can be seen.

The crust is thicker at lower latitudes, and thinner at higher latitudes and beneath some impact basins (Smith et al. 2012). Northern lowlands are apparently 2 km lower than surrounding terrain, and a broad gravity low is centered over the north pole. A mid-latitude ENE/WSW trending discontinuous upland associated with a weak positive gravity anomaly extends over half of Mercury's circumference. Regional anomalies include a locally elevated region at 68 degrees N, 33 degrees E, Caloris Basin, and the southeast rim of the Sobkou Basin. The positive free air anomaly (gravity corrected for variations in elevation relative to perfect geoid) near Sobkou is associated with the adjacent topographic rise (Fig. 2.8). The Bouguer anomaly (gravity corrected for variations in elevation and mass relative to perfect geoid) shows strong positive anomalies over Sobkou and Budh as well as Caloris,

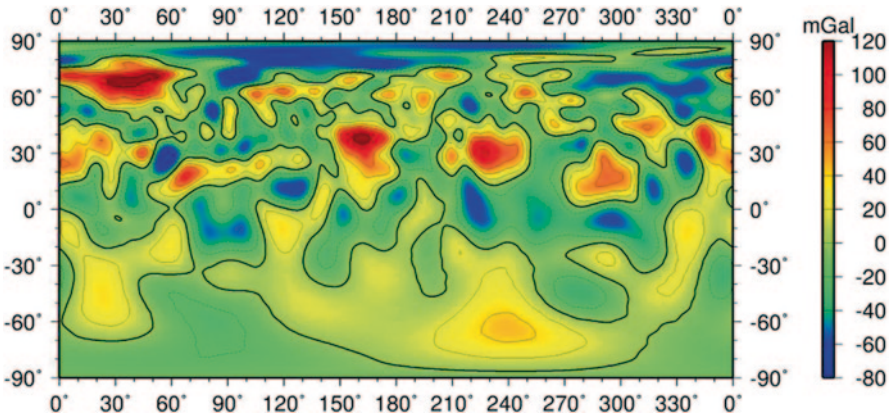


**Fig. 2.8** Gravity free air anomalies ( compensated for elevation) to harmonic order and degree 50. Note high sensitivity in northern latitudes due to lower altitude observations. (Courtesy of Mazarico et al. 2014, LPS, Fig. 3)

and a weaker negative anomaly over the rise, indicating crustal thinning beneath basins, a phenomenon associated with mascons and indicating that the crust mantle boundary is elevated beneath these basins.

As discussed above, from derivations of planetary spin parameters combined with low degree gravity field a radial density distribution model was created consistent with a solid silicate crust and mantle overlying a solid iron sulfide layer surrounding an iron-rich liquid outer core and solid inner core. Based on the bulk composition implied by the surface geochemical data, the density contrast between crust and mantle is assumed to be approximately 200 kg/m$^3$. The gravity model (Smith et al. 2012) points to an interior structure for Mercury different from those of other inner Solar System bodies, and when combined with thermal and magnetic field models suggests a solid lower density layer capping the core. Combined bulk compositional data suggest FeS for the solid 'cap' and a core with Fe alloyed with Si as well as S. A static electrically conducting layer surrounding the core decreases overall field strength and attenuates its harmonic components in a manner consistent with observations.

## 2.8 Mercury's Core

Ground-based radar, *Mariner 10,* and MESENGER observations all confirm, in various ways described here, a partially molten core. The $<1$ value of the $C_M/C$ (Smith et al. 2012) implies a liquid layer at a depth that decouples the motion of the outer shell from the interior on a time scale of 88 days, a Mercury year. Table 2.3 lists values derived for the dynamic figure properties, including oblateness, the moments of inertia values, and ellipticity, derived from MESSENGER. These agree within one standard deviation with ground-based radar derivations.

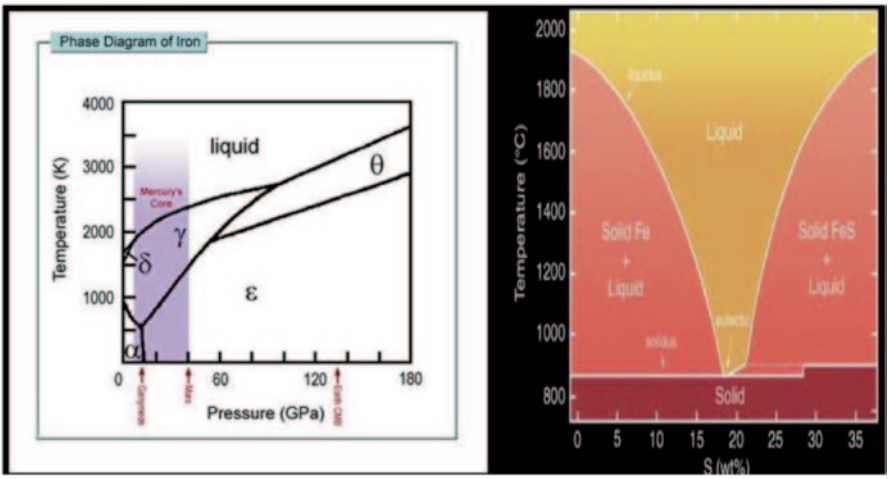


**Fig. 2.9** Simplified iron phase diagram (modified from Ahrens et al, 2002) and Fe and S system eutectic diagram. Courtesy of Diviner Team Website Mercury Poster.

Both Mercury and Earth have partially molten cores and dynamos, but with a notable difference in size between the mantles (much smaller on Mercury) and the core (much larger on Mercury), and the very different structure of Mercury's core with its outer molten layer and outer solid 'cap.' Gravity conditions correspond roughly to Mars based on core size, but Ganymede based on planet size. Hauck and coworkers (2013) described the structure of the core and internal structure in detail. The top of the liquid core is at 2020 km, with density decreasing by a factor of 2 immediately below (6980+/–280 kg/m$^3$) to immediately above (3380+/–200 kg/m$^3$) this boundary. The discontinuity is persistent for a wide range of compositions. Mercury has a solid outer shell, with a thickness of 410+/–36 km and an average density of 3650+/–225 kg/m$^3$. Observed compositions favor partitioning of Si and/or S into the metallic core during global geochemical differentiation (Hauck et al. 2013). The thermodynamic properties of a core with both Si and S suggest formation of an FeS-rich layer that is at least partially solid during the core formation process, as illustrated by the iron phase diagram (Ahrens et al. 2002), eutectic of the Fe and S system (Fig. 2.9). Increasing S abundance in the core translates into a smaller solid inner core increasing in size as a function of time (Fig. 2.10). Based on the current inner core size, a larger S abundance seems more likely.

These combined data led Hauck and coworkers (2013) to interpret the most likely core composition to be Fe-S-Si, although moments of inertia measurements are compatible with FeS, FeSi or Fe-S-Si systems (Fig. 2.11). FeSi, Fe-S-Si, and FeS vary in oxygen fugacity and reduction from most to least, respectively. FeS immiscibility and buoyancy drives the chemical segregation of a solid FeS 'cap' on the core and allows that core to remain at least partially molten to the present day, increasing the density of the outer shell. Some S partitions to silicate melt during differentiation. The immiscibility of sulfides in the core leads to the concentrated

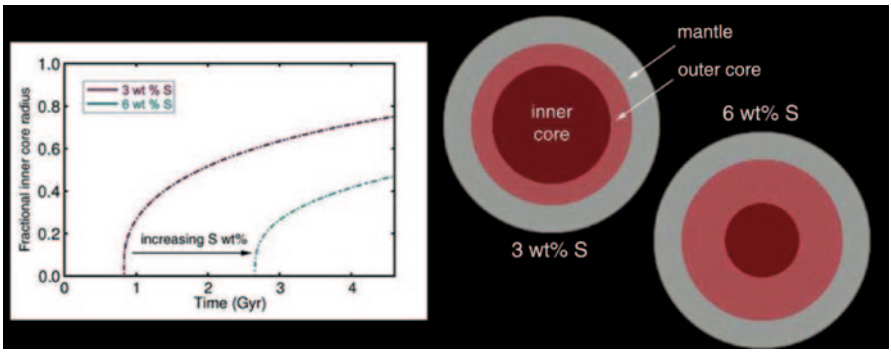


**Fig. 2.10** S abundance in the core with implications for core size as a function of time. (Courtesy of Diviner Website Mercury Poster)

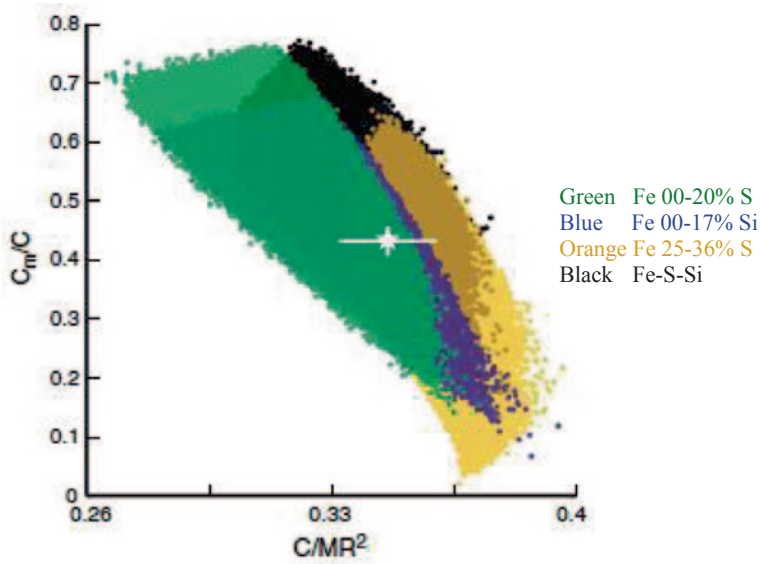


**Fig. 2.11** Core composition as a function of C/MR2 and CM/C, with key indicated on diagram. (Hauck et al. 2013, Fig. 2, © 2013 American Geophysical Union)

FeS layer on top, favoring precipitation of FeS-rich solids on top and more Si rich materials below. As the radius of the solid/liquid boundary increases, $C/MR^2$ increases, and $C_M/C$ decreases (Fig. 2.11). Increase in the solid outer shell density leads to increases in both, as it accounts for a larger proportion of the planet's mass. According to this work, earlier estimates of crust and mantle thickness were too high.

Composition stratification in the Fe-S-Si core affects magnetic field generation as well. The existence of the stable, electrically conductive layer beneath the core

mantle boundary attenuates the shorter term, and shorter wavelength components of the dynamo-generated field (Christensen 2006). The magnitude of the effect depends on the thickness and conductivity. This model is consistent with the observed long-wavelength structure of the magnetic field with apparent attenuation of higher than quadrupole harmonics (Anderson et al. 2011). The inner core must be small to allow the convecting region in the core to be of sufficient thickness. Large solubility of Si in Fe metal combined with the smaller melting point depression of FeSi systems, indicate that a core with Si could be larger than one with S alone (Hauck et al. 2004).

MESSENGER GRS-derived U and Th abundances may be too low to support strong partitioning into the core and cause additional heating. High S abundance would favor K solubility and its distribution as a radiogenic element to increase core heating and aid in dynamo generation, as well as slowing cooling and delaying the onset of the solid FeS 'cap.'

## 2.9 Internal and External Influences on Mercury's Dynamo

Conventional dynamo theory doesn't explain the weakness of Mercury's magnetic field. Heyner and coworkers (2011) proposed a feedback mechanism between the magnetic field and the magnetosphere to account for Mercury's observed weak magnetic field. The external Interplanetary Magnetic Field (IMF) contributes to both the magnetosphere and interior magnetic fields. Mercury's internally generated field lies close to the surface due to the intensity of the solar wind flux. Heyner and coworkers (2011) use magneto-hydrodynamic models to invoke coupling between Mercury's magnetosphere and internal dynamo, and found that the combination of typical IMF fields combined with Mercury's weak field matches the observations. The classical field strength saturation mechanism (Lorentz Force) is replaced by the impact of the external field. In effect, a magnetopause is created as a result of interactions between the planetary dipole field and the solar wind. According to Heyner and coworkers (2011), the external field resulting from the magnetopause current reaches into the fluid outer core, where the dynamo dipole field and external field are anti-parallel, generating anticyclones that convert the poloidal field into an azimuthal field, stretching it away from the equator, mixing and weakening both fields, and causing a less pronounced strengthening at the north pole and more uneven distribution. Heyner and coworkers (2011) also suggest that inner-core crystallization even after the planet's heat flux became sub-adiabatic, which may have revitalized Mercury's dynamo. Anderson and coworkers (2011) attempted to separate internal and external magnetic field contributions, and found that the global field is southward directed and spin aligned, with the dipole offset along the spin axis by 484+/–11 km north of the geographic equator, as discussed in Chap. 4. As a result, the magnetic field at the surface is 3–4 times larger in the northern hemisphere. The surface area open to direct magnetic flux is 4 times larger

in the southern hemisphere, which is likely to result in greater sputtering at the surface and preferential precipitation of plasmas. Saturn is similarly aligned and is offset along its dipole, but ratio of offset to diameter is 5 times greater for Mercury. Saturn's offset is thought to result from a differentially rotating conducting layer between a deeper tilted field and exterior fields, perhaps indicating an analogous mechanism for Mercury.

## References


Achille, G., Popa, C., Massironi, M., Mazzotta Epifani, E., Zusi, M., Cremonese, G., Palumbo, P.: Mercury's radius change estimates revisited using MESSENGER data. Icarus. **221**, 450–460 (2012)

Ahrens, T., Holland, K., Chen, G.: Phase diagram of iron, revised-core temperatures. Geophys. Res. Lett. **29**(7), 54-1–54-4 (2002)

Anderson, B., Acuna, M., Korth, H., Purucker, M., Johnson, C., Slavin, J., Solomon, S., McNutt, R.: The structure of Mercury's magnetic field from MESSENGER's first flyby. Sci. **321**, 82–85 (2008)

Anderson, B., Johnson, C., Korth, H., Purucker, M., Winslow, R., Slavin, J., Solomon, S., McNutt, R., Raines, J., Zurbuchen, T.: The Global magnetic field of mercury from MESSENGER orbital observations. Sci. **333**, 1859–1862 (2011)

Anderson, J.D., Jurgens, J., Lau, E., Slade, M., Schubert, G.: Shape and orientation of Mercury from radar ranging data. Icarus. **124**, 690–697 (1996)

Brown, S., Elkins-Tanton, L.: Compositions of Mercury's earliest crust from magma ocean models. Earth. Planet. Sci. Lett. **286**, 446–455 (2009)

Chen, B., Li, J., Hauck, S.: Non-ideal liquidus curve in the Fe-S system and Mercury's snowing core. Geophys. Res. Lett. **35**, L07201 (2008). doi:10.1029/2008GL033311

Christensen, U.: A deep dynamo generating Mercury's magnetic field. Nat. **105**, 1058 (2006). doi:10.1038/nature05342

Christensen, U., Wicht, J.: Models of magnetic field generation in partly stable planetary cores: applications to Mercury and Saturn. Icarus. **196**, 16–34 (2008)

Clark, P.: Mercury's interior, in dynamic planet: Mercury in the context of its environment, pp. 37–60, Springer, Berlin (2007).

Denevi, B., Robinson, M, Solomon, S., Murchie, S., Blewett, D., Domingue, D., McCoy, T, Ernst, C., Head, J., Watters, T., Chabot, N.: The evolution of Mercury's crust: a global perspective from MESSENGER. Science. **324**, 613–618 (2009)

Diviner Team: Mercury Website. http://diviner.ucla.edu/mercury/posters/Poster-13/poster-13.pdf (2012). Accessed 13 Nov 2014

Ebel, D., Alexander, C.M.: Equilibrium condensation from Chondritic porous IDP enriched vapor: Implications for Mercury and enstatite chondrites origins. Plan. Space. Sci. **59**, 1888–1894 (2011)

Evans, L., Peplowski, P., Rhodes, E., Lawrence, D., McCoy, T., Nittler, L., Solomon, S., Sprague, A., Stockstill-Cahill, K., Starr, R., Weider, S., Boynton, W., Hamara, D., Goldsten, J.: Major element abundances on the surface of Mercury: Results from the MESSENGER Gamma-ray Spectrometer. J. Geophys. Res. Planet. **117**, E00L07 (2012). doi:10.1029/2012JE004178

Gao, P., Stevenson, D.: The effect of nonhydrostatic features on the interpretation of Mercury's mantle density from MESSENGER results. American Astronomical Society DPS meeting 401.08, DPS 44 (2012)

Griffin, A.A., Millman, P.M., Halliday, I.: "The fall of the Abee meteorite and its probable orbit". R. Astron. Soc. Can. J. (ISSN 0035-872X), **86**(8), 5–14 (1992)

Grott, M., Breuer, D., Laneuville, M.: Thermo-chemical evolution and global contraction of Mercury. Earth. Planet. Sci. Lett. **307**, 135–146 (2011)

Hauck, S., Dombard, A., Phillips, R., Solomon, S.: Internal and tectonic evolution of Mercury. EPSL. **222**, 713–728 (2004)

Hauck, S., Margot, J., Solomon, S., Phillips, R., Johnson, C., Lemoine, F., Mazarico, E., McCoy, T., Padovan, S., Pele, S., Perry, M., Smith, D., Zuber, M.: The curious case of Mercury's internal structure. JGR Planets. **118**, 1204–1220 (2013)

Head, J., Chapman, C., Strom, R., Fassett, C., Denevi, B., Blewett, D., Ernst, C., Watters, T., Solomon, S., Murchie, S., Prockter, L., Chabot, N., Gillis-Davis, J., Whitten, J., Goudge, T., Baker, D., Hurwitz, D., Ostrach, L., Xiao, Z., Merline, W., Kerber, L., Dickson, J., Oberst, J., Byrne, P., Klimczak, C., Nittler, L.: Flood Volcanism in the Northern High Latitudes of Mercury revealed by MESSENGER. Science. **333**, 1853–1856 (2011)

Heyner, D., Wicht, J., Gomez-Perez, N., Schmitt, D., Auster, H.-U., Glassmeier, K.-H.: Evidence from numerical experiments for a feedback dynamo generating mercury's magnetic field. Sci. **334**, 1690–1693 (2011)

Keil, K.: Mineralogical and chemical relationships among enstatite chondrites. J. Geophys. Res. Planet. **73**, 6945–6976 (1968)

King, S.: Pattern of lobate scarps on Mercury's surface reproduced by a model of mantle convection. Nat. Geosci. **1**, 229–232 (2008). doi:10.1038/ngeo152

Kerber, L, Head, J., Solomon, S., Murchie, S., Blewett, D., Wilson, L.: Explosive volcanic eruptions on Mercury: eruption conditions, magma volatile content, and implications for interior volatiles abundances. EPS., **285**, 263–271 (2009)

Kerber, L., Head, J., Blewett, D., Solomon, S., Wilson, L., Murchie, S., Robinson, M., Denevi, B., Domingue, D.: The global distribution of pyroclastic deposits on Mercury: The view from MESSENGER flybys 1–3. Planet. Sp. Sci. **59**, 185–1909 (2011)

LeFeuvre, M., Wieczorek, M.: Nonuniform cratering of the terrestrial planets. Icarus. **197**, 291–306 (2008)

Lu, J., Sun, Y., Toksoz, M.N., Zheng, Y., Zuber, M.: Seismic effects of the Caloris basin impact, Mercury. Plan. Space. Sci. **59**, 1981–1991 (2011)

Margot, J., Peale, S., Solomon, S., Hauck, S., Ghigo, F., Jurgens, R., Yseboodt, M., Giorgini, J., Padovan, S., Campbell, D.: Mercury's moment of inertia from spin and gravity data. J. Geophys. Res. Planet. **117**, E12 (2012). doi:10.1029/2012JE004161

Mazarico, E., Genova, A., Goossens, S., Lemoine, F., Smith, D., Zuber, M., Neumann, G., Solomon, S.: The gravity field of Mercury from MESSENGER, Lunar and Planetory Science Conference, 45, 1863.pdf (2014).

McCoy, T., Dickinson, T., Lofgren, G.: Partial melting of the Indarch (EH4) meteorite: A textural, chemical, and phase relations view of melting and melt migration. Meteorit. Planet. Sci. **34**, 735–746 (1999)

McCubbin, F., Riner, M., VanderKaaden, K., Burkemper, L.: Is Mercury a volatile rich planet? Geophys. Res. Planet. **39**, L09202 (2012). doi:10.1029/2012GL051711

Michel, N., Hauck, S., Solomon, S., Phillips, R., Roberts, J., Zuber, M.: Thermal evolution of Mercury as constrained by MESSENGER observations. J. Geophys. Res. Planet. **118**, 1033–1044 (2013)

Nittler, L., Starr, R., Weider, S., McCoy, T., Boynton, W., Ebel, D., Ernst, C., Evans, L., Goldsten, J., Hamara, D., Lawrence, D., McNutt, R., Schlemm, C., Solomon, S., Sprague, A.: The major element composition of Mercury's surface form MESSENGER X-ray spectrometry. Sci. **333**, 1847–1849 (2011)

Oberst, J., Elgner, S., Turner, F.S., Perry, M., Gaskell, R., Zuber, M., Robinson, M., Solomon, S.: Radius and limb topography of Mercury obtained form images acquired during the MESSENGER flybys. Plan. Space. Sci. **59**, 1918–1924 (2011)

Peplowski, P., Evans, L., Hauck, S., McCoy, T., Boynton, W., Gillis-Davis, J., Ebel, D., Goldsten, J., Hamara, D., Lawrence, D., McNutt, R., Nittler, L., Solomon, S., Rhodes, E., Sprague, A., Starr, R., Stockstill-Cahill, K.: Radioactive elements on Mercury's surface from MESSENGER: Implications for the planet's formation and evolution. Sci. **333**, 1850–1852 (2011)

Peplowski, P., Lawrence, D., Rhodes, E., Sprague, A., McCoy, T., Denevi, B., Evans, L., Head, J., Nittler, L., Solomon, S., Stockstill-Cahill, K., Weider, S.: Variations in the abundances of potassium and thorium on the surface of Mercury: Results from the MESSENGER Gamma-ray spectrometer. J. Geophys. Res. Planet. **117**, E00L04 (2012a). doi:10.1029/2012JE004141

Peplowski, P., Rhodes, E., Hamara, D., Lawrence, D., Evans, L., Nittler, L., Solomon, S.: Aluminum abundance on the surface of Mercury: Application of a new background-reduction technique for the analysis of gamma-ray spectroscopy data. J. Geophys. Res. Planet. **117**, E00L10 (2012b). doi:10.1029/2012JE004181

Perry, M., Kahan, D., Barnouin, O., Ernst, C., Solomon, S., Zuber, M., Smith, D., Phillips, R., Srinivasan, D., Oberst, J., Asmar, S.: Measurement of the radius of Mercury by radio occultation during the MESSENGER flybys. Plan. Space Sci. **59**, 1925–1931 (2011)

Preusker, F., Oberst, J., Head, J., Watters, T., Robinson, M., Zuber, M., Solomon, S.: Stereo topographic models of Mercury after three MESSENGER flybys. Plan. Space Sci. **59**, 1920 − 1917 (2011)

Prockter, L., Ernst, C., Denevi, B., Chapman, C., Head, J., Fassett, C., Merline, W., Solomon, S., Watters, T., Strom, R., Cremonese, G., Marchi, S., Massironi, M.: Evidence for young volcanism, on Mercury from the thirds MESSENGER flyby. Science. **329**(5992), 668–671 (2010)

Purucker, M., Sabaka, T., Solomon, S., Anderson, B., Korth, H., Zuber, M., Neumann, G.: Mercury's internal magnetic field: constraints on large and small-scale fields of crustal origin. Earth. Planet. Sci. Lett. **285**, 340–346 (2009)

Redmond, H., King, S.: Does mantle convection currently exist on Mercury? Phys. Earth. Plan. Inter. **164**(3–4), 221–231 (2007)

Rhodes, L., Evans, L., Nittler, L., Starr, R., Sprague, A., Lawrence, D., McCoy, T., Stockstill-Cahill, K., Goldsten, J., Lawrence, D., McCoy, T., Stockstill-Cahill, K., Goldsten, J., Peplowski, P., Hamara, D., Boynton, W., Solomon, S.: Analysis of MESSENGER gamma-ray spectrometer data from the Mercury flybys. Plan. Space. Sci. **59**, 1829–1841 (2011)

Riner, M., McCubbin, F., Lucey, P., Taylor, G.J., Gillis-Davis, J.: Mercury surface composition: Integrating petrologic modeling and remote sensing data to place constraints on FeO abundance. Icarus. **209**, 301–313 (2010)

Roberts, J., Barnouin, O.: The effect of Caloris impact on the mantle dynamics and volcanism of Mercury. J. Geophys. Res. Planet. **117**, E02007 (2013). doi:1029/2011JE003876

Stockstill-Cahill, K., McCoy, T., Nittler, L., Weider, S., Hauck, S.: Magnesium-rich crustal compositions on Mercury: Implications for magmatism for petrologic modeling. J. Geophys. Res. Planet. **117**, E00L15 (2012). doi:10.1029/2012JE004140

Smith, D., Zuber, M., Phillips, R., Solomon, S., Neumann, G., Lemoine, F., Peale, S., Margot, J., Torrence, M., Talpe, M., Head, J., Hauck, S., Johnson, C., Perry, M., Barnouin, O., McNutt, R., Oberst, J.: The equatorial shape and gravity field of mercury from MESSENGER flybys 1 and 2. Icarus. **209**, 88–100 (2010)

Smith, D., Zuber, M., Phillips, R., Solomon, S., Hauck, S., Lemoine, F., Mazarico, E., Neumann, G., Peale, S., Margot, J.-L., Johnson, C., Torrence, M., Perry, M., Rowlands, D., Goossens, S., Head, J., Taylor, A.: Gravity field and internal structure of Mercury from MESSENGER. Sci. **336**, 214–217 (2012)

Sprague, A., Hunten, D., Lodders, K.: Sulfur at Mercury, elemental at the poles and sulfides in the regolith. Icarus. **118**, 211–215 (1995)

Sprague, A., Emery, A., Donaldson, K., Russell, R., Lynch, D., Mazuk, A.: Mercury: Mid-Infrared (3-13 u) observations show heterogeneous composition, presence of intermediate and basic soil types, and pyroxene. Meteorit. Planet. Sci. **37**, 1255–1268 (2002)

Sprague, A., Massey, S.: Mercury's exosphere: A possible source of Na. Planet. Space. Sci. **5**(11), 1614–1621 (2007)

Stevenson, D., Lunine, J.: Rapid formation of Jupiter by diffusive redistribution of water vapor in the solar nebular. Icarus. **75**, 146–155 (1988)

Weider, S., Nittler, L., Starr, R., McCoy, T., Stockstill-Cahill, K., Byrne, P., Denevi, B., Head, J., Solomon, S.: Chemical heterogeneity of Mercury's surface revealed by the MESSENGER X-ray spectrometer. J. Geophys. Res. Planet. **117**, E00L05 (2012). doi:10.1029/2012JE004153

Weider, S., Nittler, L., Starr, R., McCoy, T., Solomon, S.: Variations in abundance of iron on Mercury's surface from MESSENGER X-ray spectrometer observations. Icarus. **235**, 170–186 (2014)

Zolotov, M., Sprague, A., Hauck, S., Nittler, L., Solomon, S., Weider, S.: The redox state, FeO content, and origin of sulfur-rich magmas on Mercury. J. Geophys. Res. Planet. **118**, 138–146 (2013)

http://www.springer.com/978-1-4939-2243-7

Mercury's Interior, Surface, and Surrounding Environment
Latest Discoveries
Clark, P.E.
2015, VIII, 97 p. 54 illus., 44 illus. in color., Softcover
ISBN: 978-1-4939-2243-7